Mapping the Cloud-Driven Atmospheric Dynamics & Chemistry of an Isolated Exoplanet Analog with Harmonic Signatures

MICHAEL K. PLUMMER [ID],[1] FRANCIS P. COCCHINI [ID],[1] PETER A. KEARNS [ID],[1] ALLISON MCCARTHY [ID],[2,3]
ÉTIENNE ARTIGAU [ID],[4,5] NICOLAS B. COWAN [ID],[6,7] ROMAN AKHMETSHYN,[6] JOHANNA M. VOS [ID],[3] EVERT NASEDKIN [ID],[3]
CHANNON VISSCHER [ID],[8,9] BJÖRN BENNEKE [ID],[4] RENÉ DOYON,[4] STANIMIR A. METCHEV [ID],[10,11] JASON F. ROWE,[12] AND
GENARO SUÁREZ [ID][13]

[1]Department of Physics and Meteorology, United States Air Force Academy, 2354 Fairchild Drive, CO 80840, USA
[2]Department of Astronomy, Boston University, 725 Commonwealth Ave., Boston, MA 02215, USA
[3]School of Physics, Trinity College Dublin, The University of Dublin, Dublin 2, Ireland
[4]Départment de Physique, Université de Montréal, IREX, Montréal, QC, H3C 3J7, Canada
[5]Observatoire du Mont-Mégantic, Université de Montréal, Montréal, QC, H3C 3J7, Canada
[6]Department of Physics, McGill University, Montreal, Canada
[7]Department of Earth & Planetary Sciences, McGill University, Montreal, Canada
[8]Chemistry & Planetary Sciences, Dordt University, Sioux Center, IA 51250
[9]Center for Extrasolar Planetary Systems, Space Science Institute, Boulder, CO 80301
[10]Western University, Department of Physics and Astronomy, London, Ontario, Canada
[11]Western University, Institute for Earth and Space Exploration, London, Ontario, Canada
[12]Department of Physics & Astronomy, Bishop's University, 2600 Rue College, Sherbrooke, QC J1M 1Z7, Canada
[13]Department of Astrophysics, American Museum of Natural History, Central Park West at 79th Street, NY 10024, USA

ABSTRACT

Young planetary-mass objects and brown dwarfs near the L/T spectral transition exhibit enhanced spectrophotometric variability over field brown dwarfs. Patchy clouds, auroral processes, stratospheric hot spots, and complex carbon chemistry have all been proposed as potential sources of this variability. Using time-resolved, low-to-mid-resolution spectroscopy collected with the JWST/NIRISS and NIRSpec instruments, we apply harmonic analysis to SIMP J013656.5+093347, a highly variable, young, isolated planetary-mass object. Odd harmonics ($k = 3$) at pressure levels ($\gtrsim 1$ bar) corresponding to iron (Fe) and forsterite (Mg_2SiO_4) cloud formation suggest potential North/South hemispheric asymmetry in the cloudy, and likely equatorial, regions. We use the inferred harmonics, along with 1-D substellar atmospheric models, to map the flux variability by atmospheric pressure level. These vertical maps demonstrate robust interaction between deep convective weather layers and the overlying stratified and radiative atmosphere. We identify distinct time-varying structures in the near-infrared that we interpret as planetary-scale wave (e.g., Rossby or Kelvin)-associated cloud modulation. We detect deviations from bulk (composite) variability in water ($S/N_{max} = 14.0$), carbon monoxide ($S/N_{max} = 13.0$), and methane ($S/N_{max} = 14.9$) molecular signatures. Forsterite cloud modulation is anti-correlated with overlying carbon monoxide and water abundances and correlated with deep methane absorption, suggesting complex interaction between cloud formation, atmospheric chemistry, and temperature structure. Furthermore, we identify distinct harmonic behavior between methane and carbon monoxide absorption bands, providing evidence for time-resolved disequilibrium carbon chemistry. At the lowest pressures ($\lesssim 100$ mbar), we find that the mapped methane lines transition from absorption to emission, supporting evidence of high-altitude auroral heating via electron precipitation.

Corresponding author: Michael K. Plummer

1. INTRODUCTION

Highly variable and rapidly rotating planetary-mass objects and low-mass brown dwarfs provide the opportunity to efficiently observe dynamic gas giant exoplanet-analog atmospheres over multiple rotations, unhindered by host star contamination (Burrows et al. 2001; Faherty et al. 2016). These objects, with inferred masses ($\lesssim 15\ M_J$) overlapping the lowest mass products of stellar formation and the highest mass products of planetary formation, serve as laboratories for understanding how atmospheric circulation, cloud formation, molecular chemistry, and auroral processes interact in H/He-dominated planetary environments.

Brown dwarfs at the transition ($T_{\rm eff} \sim 1300$ K) from mineral cloud-rich late-L dwarfs to the more cloud-sparse mid-T dwarfs exhibit amplified variability (Radigan et al. 2014; Radigan 2014; Eriksson et al. 2019; Liu et al. 2024). Driving sources of this variability are believed to include multiple, patchy cloud layers perhaps of varying thickness (e.g., Ackerman & Marley 2001; Burgasser et al. 2002; Reiners & Basri 2008; Apai et al. 2013); planetary-scale waves (for e.g., Rossby or Kelvin waves, Apai et al. 2017, 2021a; Zhou et al. 2020; Fuda et al. 2024); cloud modulation driven by those planetary-scale waves (Plummer et al. 2024); double-diffusive convection tied to disequilibrium carbon chemistry (Tremblin et al. 2015, 2016); upper atmospheric hot spots (Robinson & Marley 2014; Morley et al. 2014); dynamically driven temperature variations (Showman & Kaspi 2013; Nasedkin et al. 2025); and potentially auroral processes (Hallinan et al. 2015; Kao et al. 2016, 2018; McCarthy et al. 2025; Nasedkin et al. 2025; Suárez et al. 2025).

1.1. *SIMP J0136*

SIMP J013656.5+093347.3 (hereafter SIMP J0136) (Artigau et al. 2006) is an L/T transition object (T2.5 $\pm$ 0.5) that is highly variable ($\gtrsim 2\%$) at near-infrared (NIR) wavelengths (see e.g., Artigau et al. 2009). With a mass (12.7 ± 1.0 M$_J$, Gagné et al. 2017) straddling the minimum deuterium-burning limit, it is often referred to as a planetary-mass object. A relatively young object (200 ± 50 Myr, Gagné et al. 2017) with an inferred surface gravity log(g) = 4.5 ± 0.4 (Vos et al. 2023), SIMP J0136 fits into a population of younger and lower surface gravity brown dwarfs exhibiting enhanced variability rates when compared to field brown dwarfs (Vos et al. 2022; Liu et al. 2024). SIMP J0136 has a rapid rotation rate (2.414 ± 0.078 h, Yang et al. 2016), likely contributing to amplified atmospheric dynamics (e.g., increased wind speeds, Allers et al. 2020), larger equator-to-pole cloud contrasts due to Coriolis effects (Tan & Showman 2021a,b), and auroral

emission due to a strengthened magnetic dynamo and associated currents (e.g., Kao et al. 2018).

Multi-modal observations suggest SIMP J0136's atmosphere is structured into multiple, time-varying mineral cloud layers. `Brewster` framework (Burningham et al. 2017) retrievals on spectra spanning $1 - 15\ \mu$m (Burgasser et al. 2008; Sorahana et al. 2013; Filippazzo et al. 2015) infer a thin and patchy forsterite (Mg$_2$SiO$_4$) cloud layer overlying a thicker and more spatially expansive iron (Fe) cloud deck (Vos et al. 2023). Ground-based photometry has detected phase shifts between the NIR bands, supporting ≥ 2 cloud layers (Yang et al. 2016; McCarthy et al. 2024; Plummer et al. 2024). The suspected forsterite clouds' phase (inferred via color index reddening) anti-correlation with variation in broadband NIR emission suggest planetary-scale waves may be related to cloud formation and dissipation (Plummer et al. 2024), similar to ammonia/ammonium hydrosulfide cloud modulation in Jupiter's atmosphere (e.g., Choi et al. 2013; de Pater et al. 2016; Fletcher et al. 2016, 2020).

With its ability to collect spectroscopic and photometric observations across the NIR and mid-IR spectrum, the James Webb Space Telescope (JWST) has revolutionized our understanding of substellar atmospheres like SIMP J0136. Applying a K-means cluster algorithm to time-resolved $0.8 - 11\ \mu$m spectra resulted in 9 characteristic lightcurve shapes (or clusters) for JWST NIR Spectrograph (NIRSpec, Jakobsen et al. 2022) data and 2 characteristic lightcurves for JWST Mid-IR Instrument (MIRI, Wright et al. 2023) data (McCarthy et al. 2025). These characteristic lightcurves potentially correspond to distinct atmospheric layers (i.e., iron and forsterite cloud layers and cloud-free regions, McCarthy et al. 2025). The K-means algorithm was previously applied to the WISE 1049 AB (L7.5/T0.5) binary brown dwarf system, finding 3 characteristic and spectrophotometrically-resolved lightcurve shapes for the NIRSpec data and 2 characteristic lightcurves for the MIRI data (Biller et al. 2024). A follow-on epoch of observations of WISE 1049 AB with the same instruments found similar results and tied the variation seen in the characteristic lightcurves to patchy clouds and higher-altitude hot spots (Chen et al. 2025).

The JWST Near Infrared Imager and Slitless Spectrograph (NIRISS; Doyon et al. 2023) instrument has also delivered important findings on SIMP J0136. Principal Component Analysis of NIRISS time-series spectroscopy found that rotational variability was driven by ≥ 3 spectrally distinct regions (Akhmetshyn et al. 2025), broadly agreeing with McCarthy et al. (2025)'s findings. Multi-wavelength lightcurves collected by NIRISS identified odd harmonics, suggesting

asymmetry between Northern and Southern hemispheres, and found initial evidence that broadband emission modulation from forsterite spectral regions was anti-correlated with variability in water and CO absorption lines (Akhmetshyn et al. 2025).

SIMP J0136 possesses a robust magnetic field potentially capable of strong auroral emissions. Radio observations with the Karl G. Jansky Very Large Array at 8-12 GHz detected a ~ 3000 G magnetic field (Kao et al. 2018), much stronger than Jupiter's ~ 4 G equatorial dipole field (see e.g., Barrow 1960; Acuna & Ness 1975; Connerney et al. 2018, 2022; Sharan et al. 2022). Auroral heating signatures, in the form of H_3+ emission at $\sim 3 \mu m$, have been detected in NIR observations of Jupiter's upper atmosphere (see e.g., Kim et al. 1993), but direct detection of H_3+ emission remains elusive for T dwarfs like SIMP J0136, and as discussed in Nasedkin et al. (2025), may remain so as H_3+'s quick reaction rate with water may prevent observable H_3+ emission (Pineda et al. 2024). Providing further support for Pineda et al. (2024)'s findings, recent observations of the isolated Y dwarf, CWISEP J193518.59-154620.3 (WISE J1935), found emission in the ν_3 rotational-vibrational methane band (Faherty et al. 2024), suggesting upper atmospheric auroral heating, although H_3+ emission was not detected.

Indirect detection methods for inferring the presence of auroral heating are promising. Time-resolved spectral retrievals (via `petitRADTRANS`, Mollière et al. 2019; Nasedkin et al. 2024) of the same JWST/NIRSpec data presented originally in McCarthy et al. (2025) identify a high-altitude, 265 K temperature inversion, attributed to tentative auroral heating from electron precipitation (Nasedkin et al. 2025).

1.2. *Outline*

In this work, we infer and vertically map the atmospheric harmonics in the time-resolved NIR spectra of SIMP J0136. We analyze JWST NIRISS and NIRSpec datasets, collected ~ 35 h apart from one another and originally presented in Akhmetshyn et al. (2025) and McCarthy et al. (2025) respectively, and identify connections between cloud modulation and temperature and chemical structure. The article is structured as follows: §2 describes the observational strategy and data reduction. §3 describes our harmonic model and best-fit scheme. §4 presents the inferred spectral harmonic parameters and uses the best-fit lightcurves and atmospheric models to create vertical (pressure vs. time) heat maps showing the evolution of the atmosphere of SIMP J0136 as well as spectral features' deviations from bulk atmospheric variability. §5 discusses the implications of our results for the dynamical, temperature, and chemical structure of SIMP J0136 and §6 summarizes our findings.

2. OBSERVATIONS AND DATA REDUCTION

To understand how the atmosphere of SIMP J0136 evolves in the NIR over time, we consider two epochs of observations by two JWST instruments, NIRISS and NIRSpec. NIRISS collections (GTO 1209, PI: Artigau) being made on Jul 22, 2023 from UT 05:08:28 to 09:05:07 (observational cadence: 1.96 min, total observation time: 2.62 h, Akhmetshyn et al. 2025), and NIRSpec observations (GO 3548, PI: Vos) conducted on July 23, 2023 from UT 18:40:56 to 22:05:06 (observational cadence: 1.83 s, total observation time: 2.90 h, McCarthy et al. 2025).

Figure 1 includes the mean emission spectra as well as the per pixel and binned (temporally and spectrally) signal-to-noise (S/N) ratio. The NIRSpec/Prism data received a larger increase in binned S/N compared to the NIRISS/SOSS data because of the large number of observations made in NIRSpec's Bright Object Times Series (BOTS) mode. Variability maps (also commonly known as dynamic spectra) are shown in Figure 2. The variability maps display the normalized variability at each observed wavelength over the period of observation, which are discussed further in §3 below.

Here we will give a brief overview of the observations and data reduction as they were previously presented in detail in McCarthy et al. (2025) and Akhmetshyn et al. (2025). NIRISS was used in Single Object Slitless Spectroscopy mode (NIRISS/SOSS) to collect 81, $R \sim 1200$ spectra from 0.85 to $2.83 \mu m$. In this work, we only consider wavelengths $> 1 \mu m$ due to background star contamination at shorter wavelengths. The SOSS-Inspired SpectroScopic Extraction (SOSSISSE) pipeline was implemented for data reduction (Lim et al. 2023). NIRSpec BOTS was used in Prism/CLEAR mode to collect 5726, $R = 30 - 300$ spectra from 0.6 to $5.3 \mu m$. As for NIRISS/SOSS above, only wavelengths $> 1 \mu m$ are considered. For data reduction, McCarthy et al. (2025) used the JWST Space Telescope Science Institute pipeline version 1.14.0 in default settings.

We use 118 s and 129 s temporal bins for NIRISS/SOSS and NIRSpec/PRISM respectively to create 81 time steps for each data set. It is worth noting that for the NIRSpec/PRISM dataset, this temporal binning reduces the observed % deviation by a factor of ~ 2 versus that seen in McCarthy et al. (2025) and Nasedkin et al. (2025). Both data sets use $0.05 \mu m$ spectral binning to compare spectral features at an equivalent resolution. We bin linearly (rather than logarithmically) to more precisely target specific molecular bands, and we acknowledge that the bins will become fractionally smaller at longer wavelengths.

3. MODELS & FITTING SCHEME

3.1. *Harmonic Model*

Using the Python code `Imber` (Plummer 2023, 2024) developed in Plummer & Wang (2022, 2023); Plummer et al. (2024), we fit each lightcurve with models of 2nd and 3rd
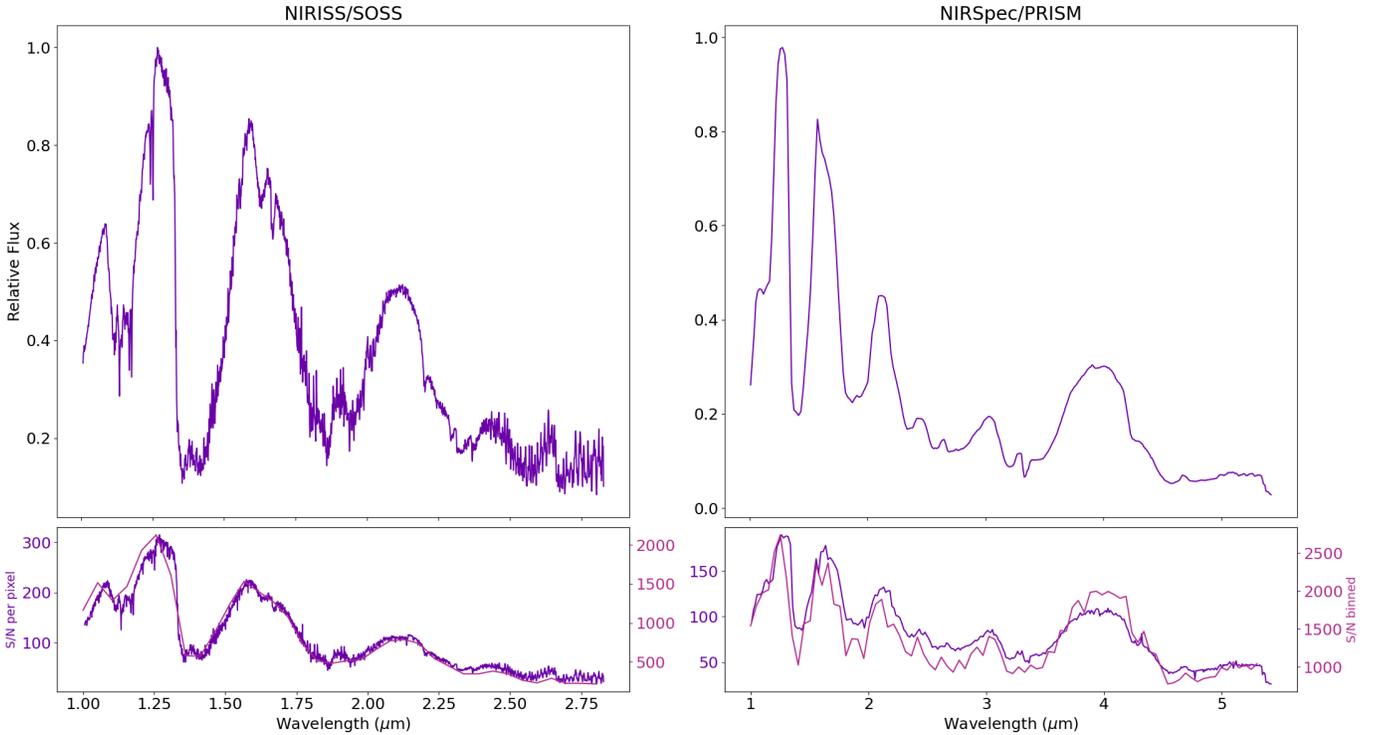
Figure 1. NIRISS/SOSS (left) and NIRSpec/PRISM (right) spectra for SIMPJ0136. **Top Row:** Time-averaged spectra normalized to maximum emission. **Bottom Row:** Per pixel (purple) and spectrally and temporally binned (magenta) signal-to-noise ratio. NIRISS/SOSS and NIRSpec/PRISM data were previously presented in Akhmetshyn et al. (2025) and McCarthy et al. (2025); Nasedkin et al. (2025), respectively.

order Fourier modes (or harmonic components), with and without damping. `Imber` is an open-source code available on GitHub[1]. The code employs Bayesian methods, specifically dynamic nested sampling (Skilling 2004, 2006; Higson et al. 2019), to find the best fit for each lightcurve using the Python module `Dynesty` (Speagle 2020). Decomposing lightcurves into their harmonic components provides the capability to directly infer parameters including amplitude, period, phase, and damping ratio for each harmonic.

We modify the harmonic model presented in Plummer et al. (2024) by adding a damping term to allow for transient atmospheric dynamics as follows,

$$F(t) = C_0 + C_1 t + \sum_i^N A_i \sin(2\pi t/P_i + \phi_i) \exp(-\lambda_i t), \quad (1)$$

where C_O is a bias, C_1 is the slope that accounts for variations on time scales that exceed the observation period, and t is time in hours. Each model is composed of the sum of N harmonic modes (the order denoted by i) for which A_i is amplitude, P_i is period, ϕ_i is phase shift, and λ_i is decay rate, which is approximated,

$$\lambda_i \approx 2\pi \zeta_i / P_i, \quad (2)$$

where ζ_i is the damping ratio for which zero indicates an undamped oscillation and values greater than one result in an overdamped wave.

3.2. *Fitting Scheme*

For the Bayesian fit, we use flat uniform priors for our free parameters: amplitude ($0\% < A_i < 5\%$), period ($0 < P_i < 3$ h), damping ($0 < \zeta_i < 1$), phase shift ($0° < \phi_i < 360°$), bias (1.0 ± 0.25), and slope ($\pm 0.1\,\mathrm{h}^{-1}$).

To determine the best-fitting model, we compare each inferred light curve's Bayesian logarithmic evidence ($\log \mathcal{Z}$) and Bayesian Information Criterion (BIC).

Bayesian evidence ($\mathcal{Z}$) derives from the denominator of Bayes' theorem,

$$P(\Theta|D,M) = \frac{P(D|\Theta,M)\, P(\Theta|M)}{P(D|M)}, \quad (3)$$

where Θ denotes inferred parameters, D represents observed data, and M the applied model. Per Bayesian standard, $P(\Theta|D,M)$ is the posterior distribution, $P(D|\Theta,M)$ is the likelihood function, $P(\Theta|M)$ is the prior distribution, and $P(D|M) = \mathcal{Z}$ is Bayesian evidence (e.g., Speagle 2020).

BIC is computed in the traditional manner (Kass & Raftery 1995),

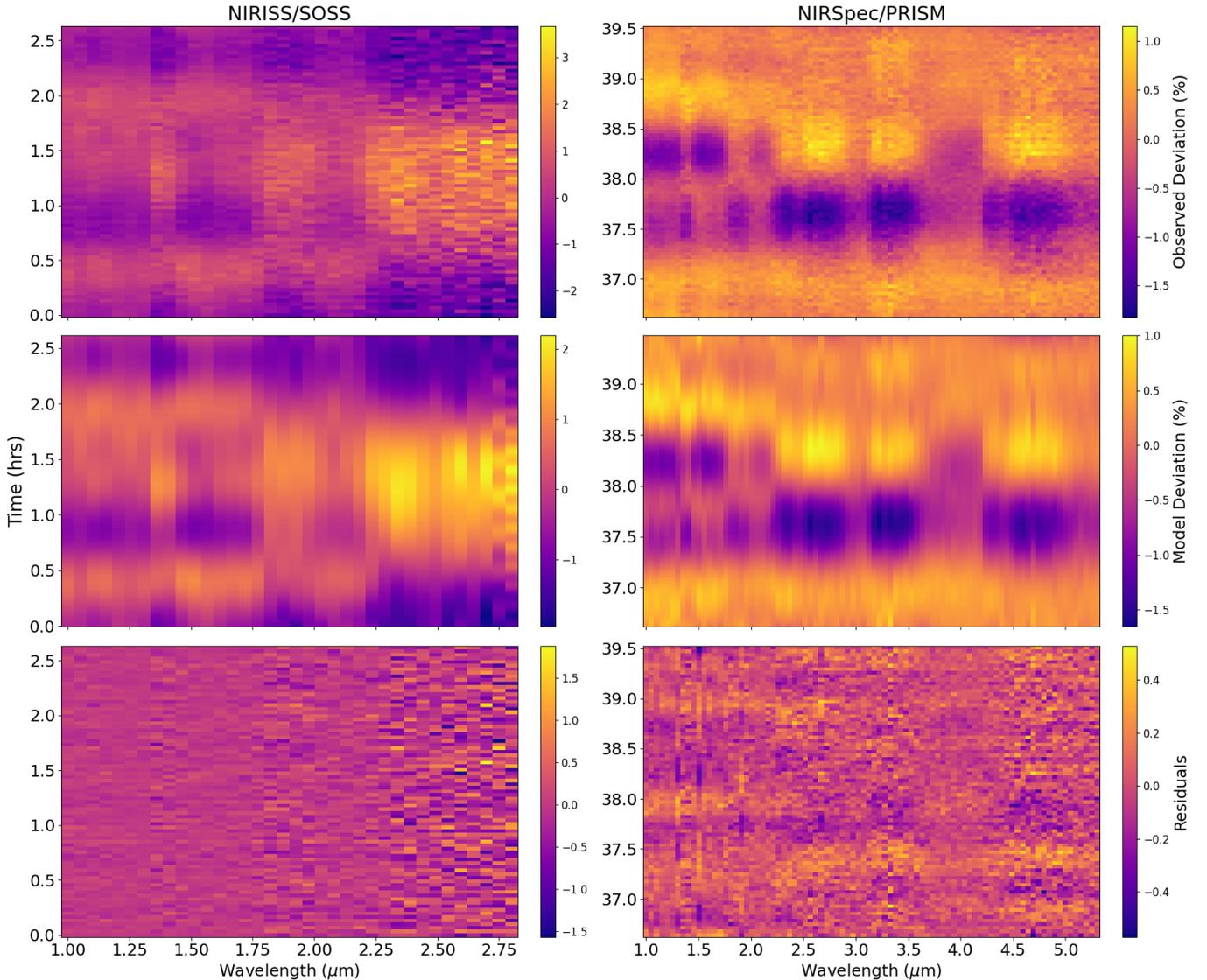$$\mathrm{BIC} = \chi^2 + m\ln(n) = \sum_{i=1}^n \frac{(O_i - M_i)^2}{\sigma^2} + m\ln(n), \quad (4)$$

Figure 2. NIRISS/SOSS (left) and NIRSpec/PRISM (right) variability maps (dynamics spectra) for SIMP J0136. Variability maps use $0.05\,\mu$m spectral binning and demonstrate the normalized spectral variability over the periods of observation. Integration times for each temporal bin are 118 s (NIRISS/SOSS) and 129 s (NIRSpec/PRISM). **Top Row:** Observed variability maps. **Middle Row:** Best-fit variability maps with lightcurves inferred using harmonic model described in §3.1 and Bayesian nested sampling. **Bottom Row:** Residuals between observed and best-fit variability maps. NIRISS/SOSS's residuals $(0.00 \pm 0.215\,\%)$ approximate white noise while the NIRSpec/PRISM residuals $(0.00 \pm 0.075\%)$ contain seemingly structured harmonics signals of $k \gtrsim 3$, likely due to unmodeled dynamics or systematics. NIRISS/SOSS and NIRSpec/PRISM data were previously presented in Akhmetshyn et al. (2025) and McCarthy et al. (2025); Nasedkin et al. (2025), respectively.

where m is the number of free parameters, n is the number of observations, O_i and M_i are the ith observation and model data, and σ is computed uncertainty. The model with the highest $\log \mathcal{Z}$ and lowest BIC value is considered the best fit.

3.3. *Best Fits*

The best-fitting models for both JWST NIRISS/SOSS and NIRSpec/PRISM data are displayed as variability maps (dynamic spectra) in the middle row of Figure 2 with residuals between the observation and best-fit models shown in the bottom row of the same figure. The NIRISS/SOSS data's larger resid-

uals $(0.00 \pm 0.215\%)$ are likely due to the data's larger variability amplitude and marginally lower binned signal-to-noise ratio. The data appears to approximate white noise but lower amplitude harmonics may be hidden. The residuals in the NIRSpec/PRISM are smaller in amplitude $(0.00 \pm 0.075\%)$ and appear to contain structured harmonics of $k \gtrsim 3$. As the Bayesian framework in `Imber` has difficulty converging on models with $\gtrsim 4$ harmonics, this signal is likely due to an unmodeled, high-order harmonic. It should be noted that the signal appears at nearly all wavelengths (and therefore pressure levels), suggesting either a source at deep pressure levels

(e.g., iron cloud modulation) or systematics. More details on the results of these fits can be found in §4.1.

3.4. *Contribution Function*

To map the inferred harmonic modes from wavelength-space to pressure-level space in §4, we use a contribution function. Contribution functions show the emitted radiation at each pressure level in wavelength-space and can be computed (Lothringer et al. 2018),

$$C(p, \lambda) = B_\lambda * \exp(-\tau_{p,\lambda}) \frac{d\tau_{p,\lambda}}{dp} \qquad (5)$$

where p is pressure, λ is wavelength, B_λ is the Planck function, and $\tau_{p,\lambda}$ is the pressure- and wavelength-dependent optical depth.

For this work, we select a cloudless, $T_{\mathrm{eff}} = 1150$ K, $\log(g) = 4.5$ Sonora Bobcat (Marley et al. 2021) contribution function (see Figures 3 and 4). The temperature and surface gravity for the model are selected based on findings of Gagné et al. (2017) and Vos et al. (2023). For similar reasons as McCarthy et al. (2025), we make the decision to use a cloudless model to probe the deepest observable pressure levels on SIMP J0136. This approach is supported by the likelihood that planetary-mass objects are composed of an admixture of cloudless and cloudy regions, based on a study of 2MASS 1207 b, an object with similar temperature and surface gravity to SIMP J0136 (Zhang et al. 2025). It should be noted that we do not necessary expect harmonic parameters to increase or decrease in the same manner as the pressure they probe (i.e., the deepest pressure should not necessarily have to have the shortest periods and lowest amplitudes).

As adapting a single contribution function may bias results (e.g., Figure 4 in Dobbs-Dixon & Cowan 2017), we compared the vertical variation maps described in §4.2.1 to maps created using the retrieved contribution function in Figure 3 of Nasedkin et al. (2025). We found that both maps contained the same key features with only minor differences that did not detract from our conclusions.

4. RESULTS

4.1. *Harmonic Analysis*

To investigate the rotational modulation and atmospheric structure of SIMP J0136, we applied 1-D harmonic wave decomposition (see §3.1) to the lightcurves obtained from both the NIRISS/SOSS and NIRSpec/PRISM instruments. By decomposing the observed variability into sinusoidal components, we retrieved wave periodicity, amplitude, phase shift, and damping ratios as a function of wavelength and associated atmospheric depth. These results allow us to examine how different spectral regions and molecular absorption (and potentially emission) features contribute to the observed spectrophotometric variability of SIMP J0136. By testing models with varying harmonic complexity, we assess the presence of layered atmospheric dynamics and chemical structures.

4.1.1. *NIRISS/SOSS Harmonic Results*

Considering NIRISS/SOSS lightcurves that span from 1.0 to 2.8 μm with 0.05 μm intervals (36 lightcurves), we identify periodic signals for each bin by fitting harmonic models using the Bayesian framework described in §3. We assume that variations in specific wavelength intervals corresponding to known molecular bands reflect variations in the absorption of those species. If the observed molecular variability was only due to the presence of clouds muting spectral features, all species would be uniformly affected. However, we see in §4.2.2 that the presence of clouds leads to enhanced absorption for methane and reduced absorption for H_2O and CO. This allows us to connect the retrieved rotational periodicities, amplitudes, and phase shifts with changes in atmospheric composition and depth.

Our harmonic analysis reveals best-fit harmonic structure varies by wavelength. Short wavelengths (1.0 to 1.45 μm) are predominantly described by three-harmonic models with mixed damping, the mid-range (1.5 to 2.1 μm) shows no strong preference between two- and three-harmonic fits, and longer wavelengths (2.15 to 2.8 μm) are consistently best fit by two-harmonic models without a systematic damping trend. Figure 3 presents retrieved periods (Top Row) and amplitudes (Bottom Row) across the NIRISS/SOSS spectral range. Points are color-coded on the basis of the dominant molecular absorption feature in each bin and inversely sized on the basis of retrieved posterior uncertainty.

The lowest-order periodicity across NIRISS/SOSS wavelengths is the $k = 1$ harmonic at $\sim$2.4 h, consistent with SIMP J0136's rotation (Yang et al. 2016). These harmonics tend to have the highest uncertainty as the period is of similar order as the observational period.

CO bands, and to a lesser extent H_2O, show retrieved periods that consistently fall between the fundamental rotation ($k = 1$, 2.4 h) and its first harmonic ($k = 2$, 1.2 h), producing beating patterns with characteristic periodicities spanning 1.2 to 2.4 h at pressure levels ranging from ~ 1 to 10^{-2} bar. These beating patterns were also seen in Apai et al. (2017, 2021b); Fuda et al. (2024) for WISE 1049 B and Zhou et al. (2022) for VHS 1256 b.

Higher-order ($k > 2$) variability traces deeper atmospheric layers as seen in Figure 3. The pressure levels associated with the maximum flux from the spectral contribution function (see §3.4) are overlaid onto the retrieved components. From 1.0 to 1.8 μm and ~ 2.0 to 2.2 μm, the $k = 3$ (0.8 h) harmonic is preferentially retrieved at pressure levels ~ 10 bar, consistent with variability originating from deeper atmospheric layers. It is noteworthy that the $k = 3$ harmonics also have the smallest posterior uncertainty.
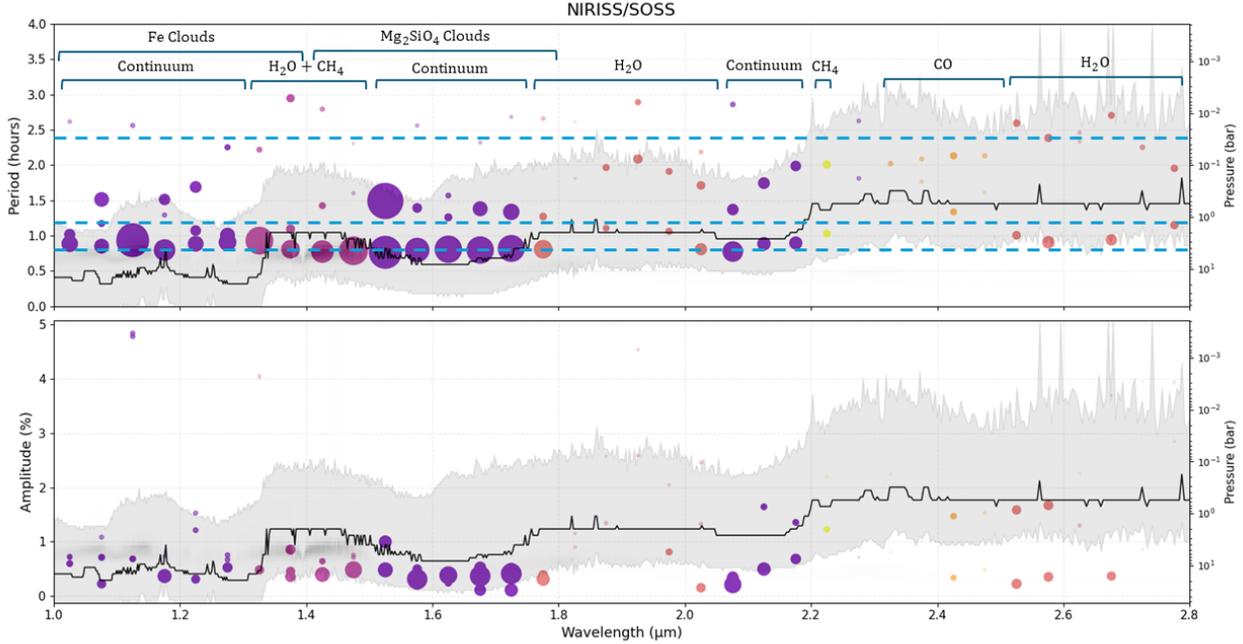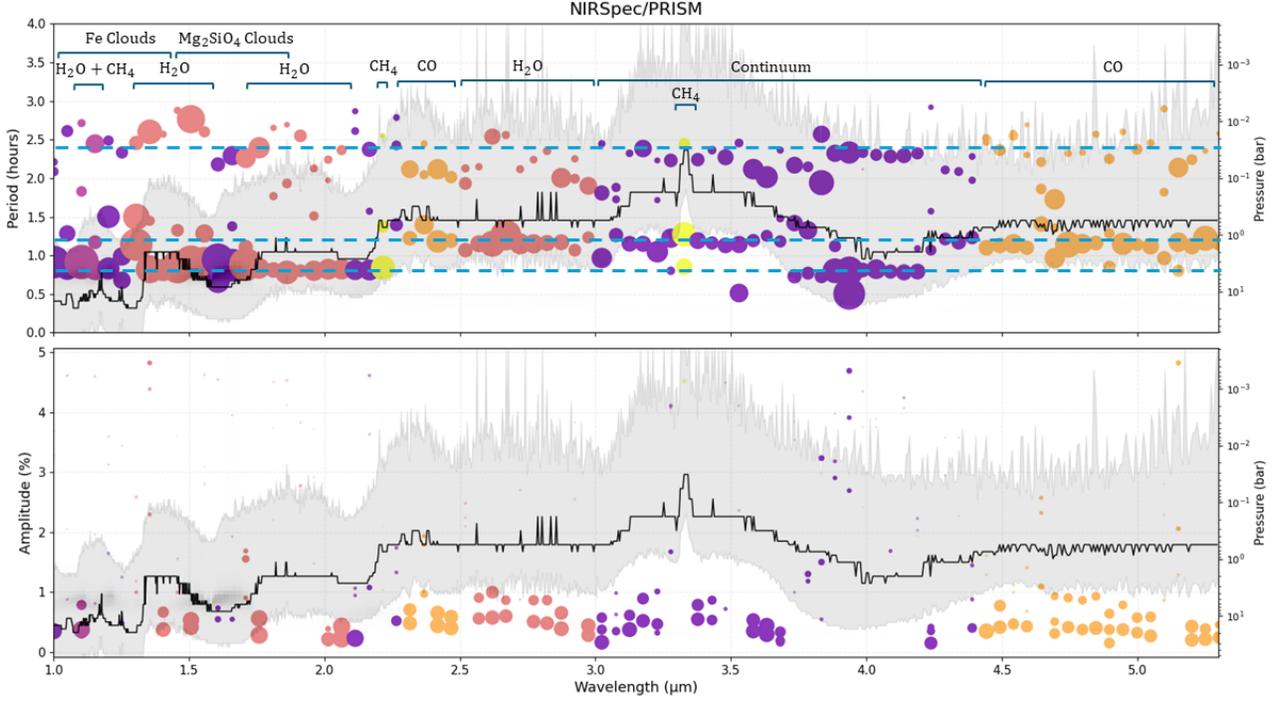
Figure 3. NIRISS/SOSS comparison of retrieved harmonic periods and amplitudes as a function of wavelength. Each data point denotes an inferred harmonic mode with either 2 or 3 modes per wavelength (contingent on the best-fit). Data points' sizes are inverse to their relative uncertainties. As seen on the left y-axis: **Top Row:** Period vs. Wavelength. It can be seen that $k = 3$ (~ 0.8 h) harmonics correspond to the deepest pressure levels ($\gtrsim 1$ bar). **Bottom Row:** Amplitude vs. Wavelength. Color denotes the dominant spectral absorption feature in each bin: Continuum (purple), $H_2O + CH_4$ (magenta), H_2O (red), CO (orange), CH_4 (yellow). The teal, dashed horizontal lines denote 2.4 h ($k = 1$), 1.2 h ($k = 2$), and 0.8 h ($k = 3$) periodicities. The black line corresponds to the maximum flux from the Sonora Bobcat (Marley et al. 2021) contribution function seen at each wavelength and the associated pressures as seen on the right y-axis. The gray shaded region represents 10^{-3} of the maximum contribution function flux.

Amplitudes are generally low across 1 to 1.8 μm ($< 1.5\%$) with isolated outliers at 1.15 and 1.35 μm. However, amplitudes increase with the onset of H_2O absorption near 1.8 μm, with both variability and uncertainties growing toward longer wavelengths. The H_2O absorption region from 2.5 to 2.8 μm reaches the highest amplitudes for the NIRISS/SOSS range.

4.1.2. *NIRSpec/PRISM Harmonic Results*

Considering a second epoch of JWST observation and extending our harmonic analysis across a wider wavelength range, we applied the same periodic modeling procedure to the lightcurves from NIRSpec/PRISM, covering 1.0 to 5.3 μm in 0.05 μm bins (86 lightcurves).

Each NIRSpec/PRISM binned lightcurve was tested to find the best-fit model (see Figure 2, Middle Row). Figure 4 presents the retrieved periods (Top Row) and amplitudes (Bottom Row) across the NIRSpec/PRISM range. Wavelengths from 1.0 to 1.5 μm were predominantly best fit by three-harmonic models. Between 1.5 to 2.1 μm, there was no strong preference between two- and three-harmonic fits, nor any consistent trend in damping configuration. For wavelengths beyond 2.1 μm, two-harmonic models became increasingly dominant.

Beating patterns with inferred periods between the $k = 1$ (2.4 h) and $k = 2$ (1.2 h) harmonics appear to be dominant from 2.25 to 3.7 μm, encompassing CO, H_2O and continuum lines, and ranging in pressure from 1 to 10^{-3} bar. The clearest beating patterns appear in the CO lines and the H_2O band between 2.5 and 3.0 μm.

The retrieved $k = 3$ harmonic is again associated with deeper layers at ~ 10 bar, consistent with NIRISS/SOSS results that locate higher-order variability at greater pressures. At pressures $\lesssim 1$ bar at 2.25 μm, models with 2 harmonics begin to dominate. Comparing the inferred amplitudes, there is increased variability in the $k = 1$ and $k = 2$ harmonics, especially in the deeper regions from 1 to 2.25 μm and the transition region from 3.5 to 4.4 μm. It should be noted that the CH_4 absorption bin at 3.3 μm is associated with the highest altitude (lowest pressure) observed from this data.

Mirroring the NIRISS/SOSS results, the H_2O absorption bands have large amplitudes; however, both the wavelengths associated with cloud modulation (1.0 to 1.8 μm) and the high-altitude continuum (~ 3.6 to 4.0 μm) also possess large amplitude waves, contrasting with the NIRISS data. The 1.8

Figure 4. NIRSpec/PRISM comparison of retrieved harmonic periods and amplitudes as a function of wavelength. Each data point denotes an inferred harmonic mode with either 2 or 3 modes per wavelength (contingent on the best-fit). Data points' sizes are inverse to their relative uncertainties. As seen on the left y-axis: **Top Row:** Period vs. Wavelength. It can be seen that $k = 2$ (~ 1.2 h) harmonics correspond to ~ 1 bar while $k = 3$ (~ 0.8 h) harmonics correspond to the deepest pressure levels ($\gtrsim 1$ bar). **Bottom Row:** Amplitude vs. Wavelength. Color denotes the dominant spectral absorption feature in each bin: Continuum (purple), $H_2O + CH_4$ (magenta), H_2O (red), CO (orange), CH_4 (yellow). The teal, dashed horizontal lines denote 2.4 h ($k = 1$), 1.2 h ($k = 2$), and 0.8 h ($k = 3$) periodicities. The black line corresponds to the maximum flux from the Sonora Bobcat (Marley et al. 2021) contribution function seen at each wavelength and the associated pressures as seen on the right y-axis. The gray shaded region represents 10^{-3} of the maximum contribution function flux.

to 3.45 μm range remains suppressed in amplitude while the CO band from 4.3 to 5.3 μm shows the smallest amplitudes.

4.2. *Vertical Variability Mapping via Harmonic Waves*

Time-resolved, multi-spectral data such as those collected by JWST NIRISS and NIRSpec instruments provide the opportunity to map the dynamic atmospheric physics of brown dwarfs and exoplanets at varying pressure levels. Using a method first demonstrated in Akhmetshyn et al. (2025), we use the best-fit harmonic models (Figure 2, Middle Row), along with a model contribution function (see §3.4), to create vertical flux variability heat maps (pressure vs. time) of the atmosphere of SIMP J0136. These vertical variability maps demonstrate the flux variability at each atmospheric layer, the interaction between layers, and unique spectral contributions to the object's dynamic atmosphere.

4.2.1. *Composite Vertical Variability Maps*

To build composite vertical variability maps, we start by scaling the model contribution function, $C(\lambda, p)$, see Equation 5, by the normalized best-fit lightcurve model, $F(\lambda, t)$, see Equation 1, for each spectral bin, $\Delta\lambda$, and time-step. At

each pressure level, p_i, we then numerically sum the scaled spectral contribution across N_λ wavelength bins to compute the pressure- and time- dependent variability,

$$V(p_i, t) = \sum_j^{N_\lambda} C(p_i, \lambda)F(\lambda, t)\Delta\lambda_j, \qquad (6)$$

resulting in a 1-D flux array in pressure-level space. The computation is then repeated at each time-step, followed by normalization of flux at each pressure level, resulting in a composite vertical variability map (Figure 5, Top Row) in terms of % deviation. The composite % deviation maps broadly match the dynamic spectra (variability maps) in Figure 2, and the vertical variability maps can be seen as a coordinate transformation of the flux heat map from time vs. wavelength to time vs. pressure.

To quantify the significance of the observed features in the retrieved maps, we scale the composite variability map (Figure 5, Top Row) by the S/N in pressure vs. time space (Figure 5, Top Row). The S/N map is computed in a similar manner as the composite map, using Equation 6, but the normalized lightcurve flux is replaced with the S/N for

each spectral bin and time-step. Comparing the S/N values in Figure 5, Bottom Row to the binned values in Figure 1, Bottom Row, shows agreement for both NIRISS/SOSS and NIRSpec/PRISM datasets. The resulting S/N-weighted map (Figure 5, Bottom Row) shows the highest deviation (ΔS/N) in the deeper pressure levels ($\gtrsim 1$ bar) due to the high S/N in these regions. The shallow layer ($\lesssim 1$ bar) exhibits smaller ΔS/N due to its lower S/N despite possessing larger % deviation.

SIMP J0136's composite vertical variability maps of the NIRISS/SOSS and NIRSpec/PRISM data reveal both similarities in the atmospheric structure observed at each epoch and apparent qualitative differences between the two observations (separated by ~ 35 h or ~ 15 rotations). Both NIRISS/SOSS and NIRSpec/PRISM maps show two dynamic interacting atmospheric layers with time-varying boundaries: (1) a lower pressure (higher altitude) overlying layer comprised of lower order harmonics and (2) a deeper layer ($\gtrsim 1$ bar) corresponding to expected cloud formation regions of forsterite and potentially iron (see e.g., Vos et al. 2023; McCarthy et al. 2024, 2025). The time-varying pressure level boundary between the deep and overlying atmospheric layers suggests variations in vertical cloud structure.

However, visual differences between the two observations' maps can be seen, suggesting complex weather patterns evolving over a relatively short timescale. In the NIRISS/SOSS observation, the deep layer's harmonic pattern is alternating single peaks of minima-maxima-minima followed by a double-peaked maximum. For the NIRSpec/PRISM observation, there are two pairs of double-peaked minima and maxima. The overlying layer evolves in complexity with the NIRSpec/PRISM observation, including a double-peaked maxima not observable in the NIRISS/SOSS data. Note that the NIRSpec/PRISM data extend to longer wavelengths and, therefore, lower pressure levels than the NIRISS/SOSS. As a result, the overlying layer in the NIRSpec/PRISM observation possesses more retrieved structure.

4.2.2. *Spectral Features' Deviations from Bulk Variability*

The broad NIR spectral coverage of JWST NIRISS/SOSS and NIRSpec/PRISM allows us to map spectral features' deviations from bulk (or composite) variability and investigate that deviation's ties to distinct atmospheric phenomena. For example, we can determine how wavelengths corresponding to iron (1.0 to 1.4 μm) and forsterite (1.4 to 1.8 μm) cloud modulation (Vos et al. 2023; McCarthy et al. 2025) or known molecular absorption bands (H_2O, CO, CH_4) deviate from bulk variability over the period of observation.

Maps depicting specific spectral regions' deviations from bulk variability can be seen in Figure 6. These maps are created by starting with the composite map (Figure 5) and then subtracting from it a second map comprising the wavelengths

available for which we are not interested for a particular test, resulting in a spectrally-unique, % deviation map. This % deviation map is then scaled by the average S/N for the wavelengths of interest. To maximize the S/N, an additional round of harmonic fitting was performed with 8.71 min temporal binning (for both observations) and spectral binning based on the entire wavelength region of interest (e.g., 1.4 to 1.8 μm for forsterite clouds).

It is important to note that maps showing deviations of individual spectral features from the bulk variability do not necessarily indicate bona fide, feature-specific variability. Rather, they reflect differences in the flux relative to the composite (bulk) signal. For example, a molecular absorption band may exhibit no intrinsic time-dependent behavior, but if bulk variability is subtracted from the spectral band light curves, the residuals would exhibit an induced anti-correlation. Nevertheless, these deviations from the bulk variability are indeed meaningful, as they highlight wavelengths with distinct morphologies from the overall spectrum.

The deviation maps for wavelengths expected to correspond to mineral cloud modulation (i.e., iron and forsterite, Vos et al. 2023) demonstrate clear harmonic patterns for both the NIRISS/SOSS and NIRSpec/PRISM datasets (see Figure 6, Top Row). The lower layer ($\gtrsim 3$ bar) is suspected to be iron cloud modulation with maximum signal-to-noise (S/N$_{max}$) deviations of 18.5 for NIRISS/SOSS and 16.1 for NIRSpec/PRISM observations. The upper forsterite layer (centered at ~ 1 bar) is approximately anti-correlated with the underlying iron layer and has S/N$_{max}$ deviations of 16.3 and 26.5 for NIRISS/SOSS and NIRSpec/PRISM respectively.

For the forsterite variation, the NIRISS/SOSS data include a double-peaked dark patch but the NIRSpec/PRISM observations contain only a single dark patch. The iron cloud regions do not appear to possess double-peaked features. For these maps, the dark and bright patches are presumed to be longitudes of enhanced or reduced cloud coverage, respectively, and will be discussed further in §5.2.

Deviation with S/N$_{max}$ = 5.5 (NIRISS/SOSS) and 14.0 (NIRSpec/PRISM) in wavelengths corresponding to dominant H_2O absorption bands (1.8 to 2.05 μm, 2.5 to 2.8 μm for NIRISS/SOSS and 2.5 to 3.0 μm for NIRSpec/PRISM) is anti-correlated with the suspected 1.4 to 1.8 μm forsterite cloud modulation for both data sets (see Figure 6, Second Row). H_2O dark spots (enhanced absorption regions) anti-correlate with the 1.4 to 1.8 μm dark spots while H_2O bright spots (reduced absorption regions) correlate with the 1.4 to 1.8 μm dark spots. H_2O deviations are strongest (highest S/N) at the ~ 1 bar pressure level, and are constrained to $\gtrsim 100$ mbar in the NIRSpec/PRISM data, but are relatively unconstrained in terms of a lower pressure bounds for NIRISS/SOSS data due to limited wavelength coverage.
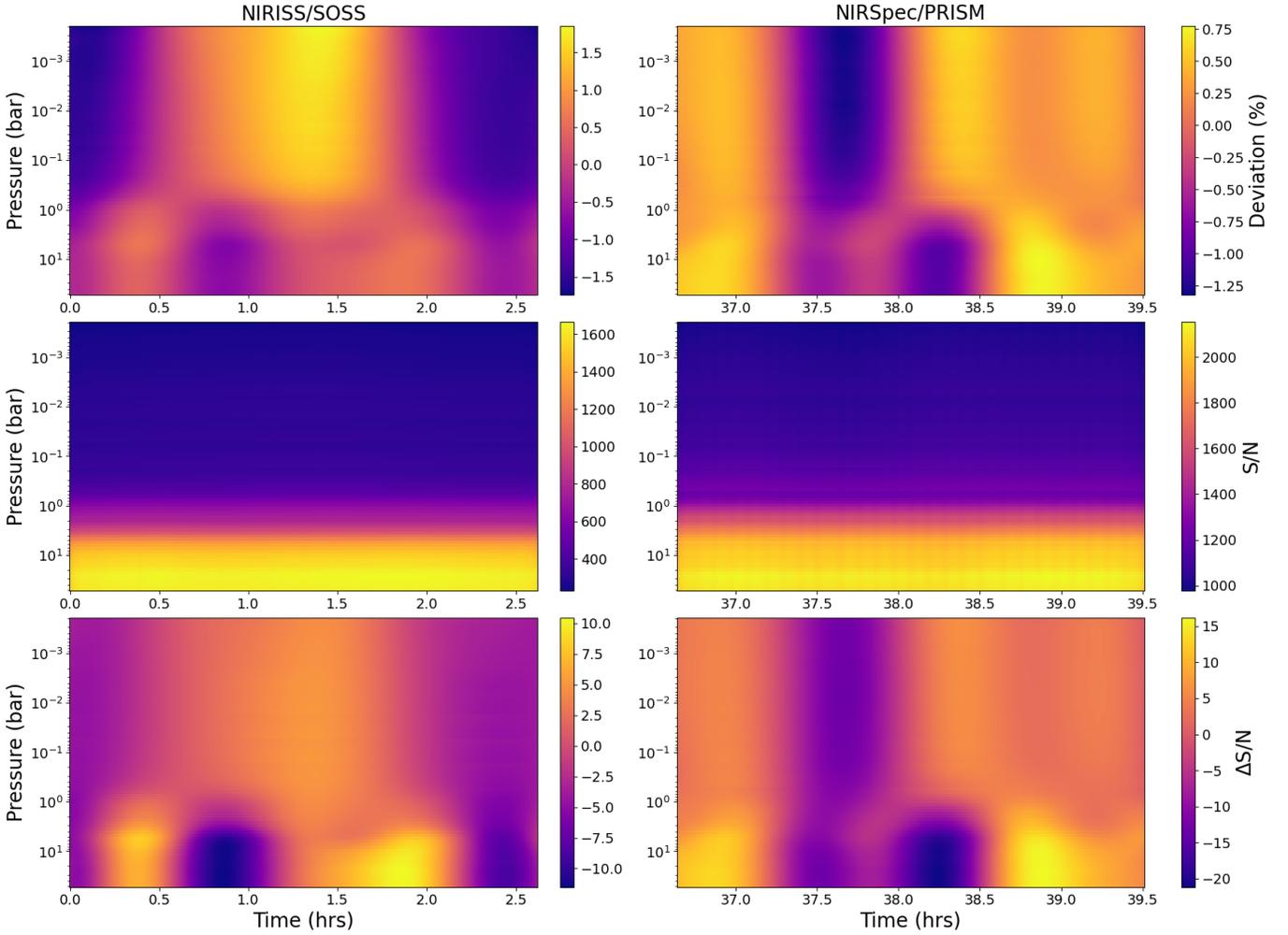
Figure 5. NIRISS/SOSS (left) and NIRSpec/PRISM (right) vertical variability maps for SIMP J0136. (Top Row) Composite maps including variation in % deviation across all observed wavelengths. (Middle Row) S/N vertical map. Pressure levels $\gtrsim 1$ bar have the highest S/N corresponding to higher observational S/N in wavelengths $\lesssim 1.8 \ \mu$m (Bottom Row) S/N-weighted composite variability maps. Stratification into $\gtrsim 2$ interacting layers can be observed. As rotational period is ~ 2.4 h, longitudinal wrapping can be observed within each observation. Visually, atmospheric evolution can be seen over the ~ 35 h between observations.

Similar to H_2O, deviations in the CO absorption bands (2.3 to 2.5 μm, with the NIRSpec/PRISM map also including the 4.4 to 5.1 μm CO band) are anti-correlated with the 1.4 to 1.8 μm modulation and show the strongest deviations at the ~ 1 bar pressure level (Figure 6, Third Row). Evidence for deviation is marginal (S/N$_{max}$ = 2.78) for the NIRISS/SOSS data but strong (S/N$_{max}$ = 14.0) for NIRSpec/PRISM observations. The NIRISS/SOSS map extends up to the 1 mbar level with a wedge-like pattern. The NIRSpec/PRISM map, on the other hand, is constrained to ~ 1 bar pressure levels. This difference is again likely due to the constraining effect of the wider spectral coverage of NIRSpec/PRISM.

As opposed to the H_2O and CO maps, the wavelengths corresponding to lower-altitude (deeper pressure levels) CH_4 absorption bands (1.1 to 1.2 μm, 1.65 to 1.75 μm, 2.15 to 2.25 μm) are correlated with 1.4 to 1.8 μm modulation in both observations (see Figure 6, Fourth Row). Evidence for

lower-altitude CH_4 deviation is weaker than for H_2O and CO, with marginal evidence (S/N$_{max}$ = 2.9) for NIRISS/SOSS data and tentative evidence (S/N$_{max}$ = 3.6) for the NIRSpec/PRISM maps. As with the CO maps, the NIRISS/SOSS deviations extend up to the 1 mbar level while the NIRSpec/PRISM deviations are constrained to the ~ 1 bar pressure level.

As the NIRSpec/PRISM data extends to 5.3 μm, it provides access to higher-altitude spectral features (as shown in the contribution function in Figures 3 and 4). The wavelengths from 3.05 to 3.5 μm bracket a CH_4 feature reaching $\lesssim 1$ mbar pressure levels. The high-altitude CH_4 map (see Figure 6, Fifth Row) has a distinct (and potentially anti-correlated) deviation pattern (S/N$_{max}$ = 14.9) compared to the lower-altitude CH_4 absorption bands. Longer wavelengths also include the relatively high-altitude spectral continuum (3.05 to 3.15 μm, 3.6 to 3.8 μm, see Figure 6, Bottom Row) with deviations (S/N$_{max}$ = 6.0) appearing to be correlated with the 1.4 to
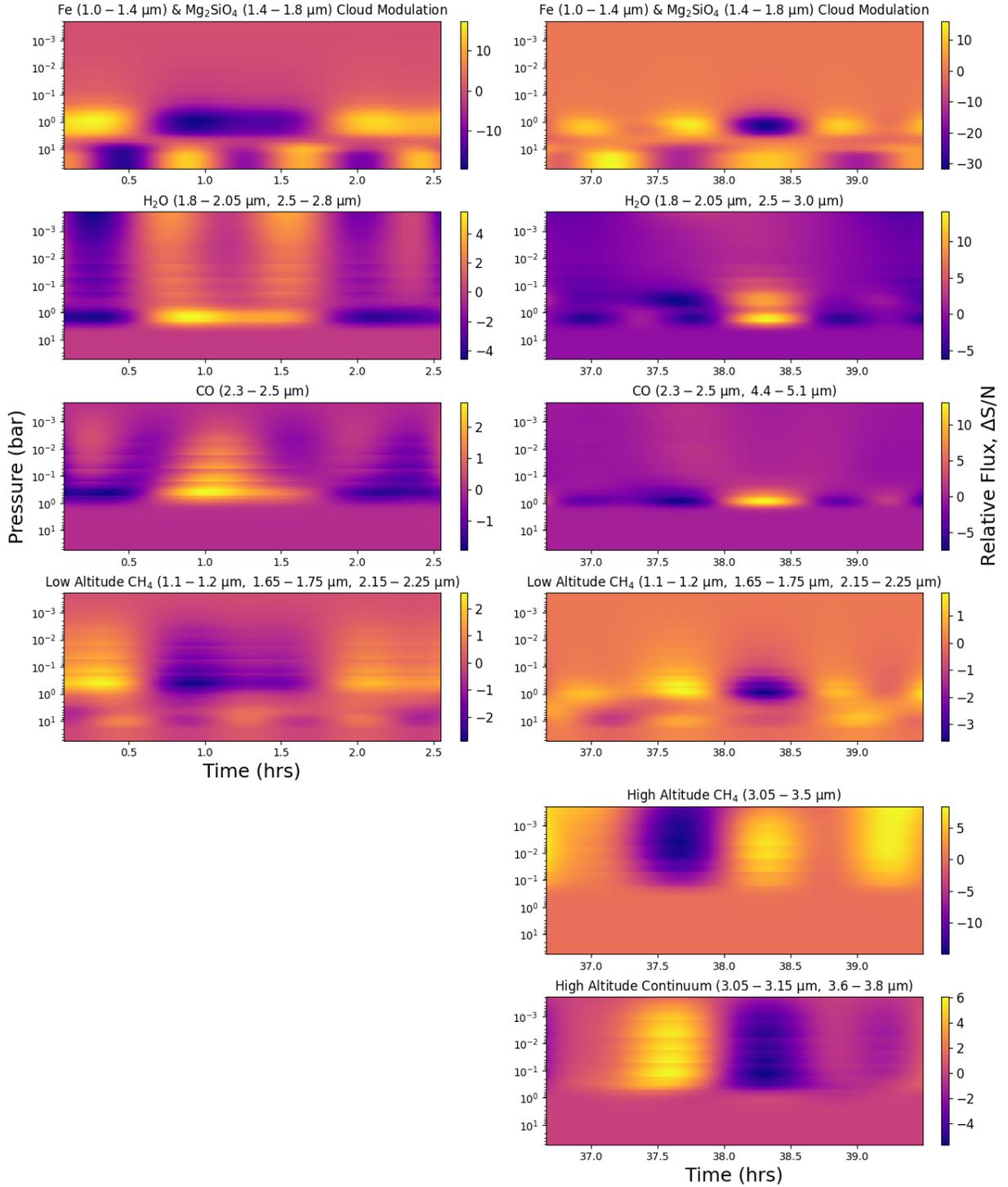
Figure 6. NIRISS/SOSS (left) and NIRSpec/PRISM (right) spectral features' deviations from bulk variability for SIMP J0136. **Top Row:** Presumed iron (lower layer, 1.0 to 1.4 μm) and forsterite (upper layer, 1.4 to 1.8 μm) cloud modulation. Wavelengths based on models and previous observations of cloud-influenced pressure levels and wavelengths for SIMP J0136 (see e.g., Vos et al. 2023; McCarthy et al. 2025). **Second Row:** H_2O deviation map; anti-correlated with forsterite cloud modulation. **Third Row:** CO deviation map; anti-correlated with forsterite cloud modulation. **Fourth Row:** Low-altitude CH_4 deviation map; correlated with forsterite cloud modulation. **Fifth Row:** (NIRSpec/PRISM only) High-altitude CH_4 deviation map. Deviation possesses similar harmonic periodicity of low-altitude CH_4 feature above cloud tops but with reverse sign, tentatively indicating emission at higher altitudes. **Bottom Row:** (NIRSpec/PRISM only) High-altitude continuum deviation; correlated with forsterite cloud modulation.

1.8 μm modulation and anti-correlated with high-altitude CH_4 deviations.

5. DISCUSSION

5.1. *Odd Harmonics in the Forsterite Cloud Layer*

Odd ($k = 3$) harmonics in SIMP J0136's spectrophotometry (see Figures 3 and 4, Top Row) are preferentially found at wavelengths corresponding to the deepest probed pressure layers as well as iron and forsterite cloud modulation (1.0 to 1.8 μm). In the NIRSpec/PRISM data set, the wavelengths expected to be most affected by cloud modulation (1.0 to 1.8 μm) and the 3.75 to 4.2 μm continuum also show high variability, suggesting the longer-wavelength continuum may be driven by the underlying cloud layer.

As initially reported by Akhmetshyn et al. (2025), odd ($k \geq 3$) harmonics in the NIRISS/SOSS data may indicate North/South asymmetry in the surface brightness map of SIMP J0136 (depending on the limb darkening law; Luger et al. 2021). In the absence of limb darkening, even spherical-harmonic degrees (l) paired with odd azimuthal orders m (which correspond to the longitudinal wavenumber k) signify a North–South asymmetry in the surface-brightness distribution (Cowan et al. 2013), an assumption adopted by Akhmetshyn et al. (2025). The situation changes, however, once limb darkening is included: linear and quadratic limb–darkening laws effectively increase the contributing spherical-harmonic degree l by one and two, respectively (Luger et al. 2021). Consequently, a linear limb–darkening law can generate apparent odd-m (odd-k) signals even for a North–South symmetric map, whereas under a quadratic law—or in the limit of negligible limb darkening—the presence of such odd modes once again implies genuine hemispheric asymmetry. Additional constraints on the limb–darkening characteristics of SIMP J0136 and similar objects will therefore be essential for robust interpretation of their light-curve morphologies.

If the odd harmonics are indeed due to North/South asymmetry, then they also support an inclined viewing geometry (Cowan et al. 2013), consistent with the estimate of $80° \pm 10°$ (Vos et al. 2017). Furthermore, this asymmetry could help lift hemispheric ambiguity in future Doppler imaging efforts with ELT-class telescopes with high-resolution spectrographs (see e.g., Plummer & Wang 2023), making SIMP J0136 an ever more compelling target for such work.

Because brown dwarfs have been found to be redder, and therefore cloudier, at equatorial latitudes than polar ones (Vos et al. 2017; Suárez & Metchev 2022; Suárez et al. 2023), the odd harmonics at the deepest pressure levels (corresponding to the cloud formation region) potentially suggest the North/South asymmetry may lie in the mineral cloud modulation region and be concentrated near the equator. Multi-rotational NIR spectroscopic observations of SIMP J0136 would help to constrain higher order odd harmonics, decrease the uncertainty in retrieved harmonic parameters, and elucidate the dynamical structure of L/T transition objects.

5.2. *Cloud-Driven Temperature and Chemical Structure*

The anti-correlation between the 1.4 to 1.8 μm forsterite cloud modulation region and H_2O and CO absorption bands, as well as the correlation of CH_4 with the same cloud region (see Figure 6), suggests that forsterite clouds influence the atmospheric chemical structure of SIMP J0136, potentially by driving variations in temperature structure and chemical mixing ratios. H_2O and CO_2 display reduced absorption at and above the cloud formation level while CH_4 exhibits enhanced absorption. The differing behavior of CH_4 implies that the explanation for the anti-correlation of H_2O and CO_2 deviations with the cloud layers cannot be completely explained due to clouds muting the observability of these absorption features.

We suggest two potential causes for the relationship between the deviations in the cloud modulation region and molecular absorption bands: (1) Cloud modulation influences the temperature structure, and therefore, the chemical conditions of the atmosphere and (2) Cloud formation and dissipation controls the oxygen abundances at co-altitude and overlying pressure levels. Both mechanisms could play a part in determining the dynamic and chemical structure of the upper atmosphere of SIMP J0136.

Forsterite cloud modulation can be seen to drive the upper atmosphere temperature structure as shown by the correlation between the dark cloud feature in Figure 6 (Top Row, Right Column) and the high-altitude continuum in Figure 6 (Bottom Row, Right Column). Regions above the clouds are relatively cooler while gaps in the cloud layer allow heat to escape initially in vertical columns (see e.g., Showman et al. 2019; Tan & Showman 2021a,b). As CO is the preferred carbon reservoir at higher temperatures (and contrastingly CH_4 is the preferred reservoir at lower temperatures), cooler regions should exhibit depleted CO and enhanced CH_4 absorption, matching our findings (Figure 6, Third and Fourth Rows) and contributing to carbon disequilibrium chemistry in SIMP J0136.

To understand the H_2O deviations in this context, we should consider the following equation (e.g., Visscher & Moses 2011),

$$CO + 3H_2 \leftrightarrow CH_4 + H_2O. \tag{7}$$

Assuming an equilibrium condition, as CO is removed from the atmosphere, the balance of the equation shifts to the left, depleting H_2O abundances.

The sequestration of oxygen in the forsterite cloud formation process may also factor into the observed anti-correlation of the cloud layer and CO/H_2O. The chemistry governing the forsterite cloud formation process can be understood by the net thermochemical reaction (e.g., Visscher et al. 2010),

$$2Mg + 3H_2O + SiO = Mg_2SiO_4(s,l) + 3H_2, \tag{8}$$

where s and l respectively denote a solid or liquid phase. The process consumes H_2O to form forsterite, potentially explaining the anti-correlation seen in Figure 6 (Second Row). Depleted oxygen abundances at and above the cloud layer also favor CH_4 over CO as the preferred carbon reservoir (see Equation 7), again explaining the observed carbon disequilibrium chemistry in SIMP J0136 as well as the chemical deviation patterns in Figure 6 (Third and Fourth Rows).

5.3. *High-Altitude Heating Source*

Mapping the deviations in the wavelengths (3.05 to 3.5 μm) bracketing the high-altitude, ν_3 rotational-vibrational CH_4 band (~ 3.4 μm, see Figure 6, Fifth Row) results in harmonics distinct from and largely anti-correlated with the low-altitude CH_4 bands (see Figure 6, Fourth Row). For example, the CH_4 absorption feature between 38.0 and 38.5 hr on the low-altitude CH_4 map is replaced by a bright spot, which we tentatively interpret as an emission feature in the upper atmosphere, potentially driven by auroral heating from electron precipitation (e.g., Sandel et al. 1982; Melin et al. 2011; Müller-Wodarg et al. 2012; Pineda et al. 2024; McCarthy et al. 2025; Nasedkin et al. 2025). In this case, the CH_4 abundance appears variable and is influenced and in-phase with underlying cloud modulation, but now we detect the CH_4 in emission rather than absorption.

Distinct, high-altitude CH_4 emission also aligns with previous findings for SIMP J0136 based on the same NIRSpec/PRISM dataset explored in this work. K-means clustering identified unique lightcurve morphology near the CH_4 ν_3-band (McCarthy et al. 2025), and a 265 K temperature inversion was inferred at pressures ($\sim 10^{-3}$ bar) corresponding to the same wavelengths (Nasedkin et al. 2025). The necessary power to create such a strong temperature inversion from electron precipitation-driven auroral heating (which is similar in strength to the 300 K heating found for WISE J1935, Faherty et al. 2024), was computed to be $\sim 10^{19}$ W by Nasedkin et al. (2025) while Jupiter-like auroral processes could only produce auroral power on the scale of 10^{17} W.

As discussed in Nasedkin et al. (2025), other upper atmospheric heating processes such as the breaking of gravity waves (Freytag et al. 2010) and Joule heating associated with atmospheric electric currents have been proposed for brown dwarfs based on observations of these mechanisms in outer solar system planets (Cowley et al. 2004; Ingersoll et al. 2021; Brown et al. 2022). Further studies will be necessary to break the degeneracies between these potential heating sources.

6. SUMMARY

To understand how mineral cloud modulation, disequilibrium carbon chemistry, and upper atmospheric heating (potentially aurora-driven) each contribute to the well-established NIR variability of the isolated L/T transition, planetary-mass

object SIMP J0136, we analyzed time-resolved spectroscopy gathered from JWST NIRISS and NIRSpec instruments, collected ~ 35 h apart, and originally presented in Akhmetshyn et al. (2025) and McCarthy et al. (2025). Performing Bayesian, Fourier fitting via `Imber`, a Python code developed in Plummer & Wang (2022, 2023); Plummer et al. (2024), we found the dominant harmonic modes (and associated parameters) for each 0.05 μm bin. Using these inferred harmonic modes and Sonora Bobcat (Marley et al. 2021) atmospheric models, we computed vertical variability maps demonstrating the flux variability at each pressure level and deviations from bulk variability for molecular absorption features (i.e., H_2O, CO, and CH_4). We summarize our findings:

1. SIMP J0136's spectral variability appears to evolve over a period of ~ 35 h (see §4.1.1, 4.1.2 and Figures 3 and 4). NIRISS/SOSS spectra show the highest variability ($2.5 - 5\%$) in H_2O absorption bands (1.75 to 2.05 μm and 2.5 to 2.8 μm) with muted variability at other wavelengths. However, NIRSpec/PRISM spectra have the highest variability at wavelengths < 2 μm (corresponding to wavelengths expected to be affected by iron and forsterite cloud modulation and including the H_2O absorption band) and also the longer-wavelength continuum (3.75 to 4.2 μm) corresponding to deep pressure levels. We interpret this variation as dynamic modulation of the forsterite cloud-forming region.

2. Harmonics with periodicities of $\lesssim 0.8$h ($k \gtrsim 3$) are inferred preferentially at pressure levels corresponding to $\gtrsim 1$ bar (the suspected iron and forsterite cloud modulation region, see §4.1.1, §4.1.2, §5.1 and Figures 3 and 4). As odd ($k \geq 3$) harmonics are potentially indicative of North/South surface map asymmetry (depending on the limb darkening law) and equatorial latitudes are known to be cloudier in brown dwarfs, the observed $k = 3$ harmonics may suggest such an asymmetry is primarily contained to the cloud-forming (and likely near-equatorial) regions.

3. We detect deviations from the bulk (composite) variability for H_2O (S/N$_{max}$ = 14.0), CO (S/N$_{max}$ = 13.0), and CH_4 (S/N$_{max}$ = 14.9) molecular absorptions bands (see Figure 6). We find modulation in the wavelengths associated with the suspected forsterite cloud layer to be anti-correlated with wavelengths corresponding to H_2O and CO and correlated with low-altitude CH_4 and upper atmospheric temperature (see §4.2.2, §5.2 and Figure 6). We suggest that cloud formation drives the temperature and chemical structure in the overlying atmosphere, leading in part to oxygen sequestration and disequilibrium carbon chemistry in the upper atmosphere.

4. We infer harmonic modes associated with the high-altitude, CH_4 rotational-vibrational ν_3 band distinct from those found in lower-altitude CH_4 band wavelengths (see §4.2.2, §5.3 and Figure 6). Although the periodicities in both inferred vertical variability maps are comparable, they are anti-correlated, with the lower-altitude presumed CH_4 absorption features transitioning to emission features. We interpret this emission as upper atmospheric heating (potentially of auroral origin) with a periodicity set by the CH_4 abundance deviations, which appear to be influenced by forsterite cloud modulation (as discussed in §5.2).

Follow-on, multi-rotational and time-resolved spectroscopy of SIMP J0136 and other highly variable brown dwarfs and directly-imaged gas giant exoplanets will be necessary to draw large-scale conclusions on the connection between cloud formation, atmospheric chemistry, and temperature structure in substellar objects.

REFERENCES

Ackerman, A. S., & Marley, M. S. 2001, ApJ, 556, 872, doi: 10.1086/321540

Acuna, M. H., & Ness, N. F. 1975, Nature, 253, 327, doi: 10.1038/253327a0

Akhmetshyn, R., Artigau, E., Cowan, N. B., et al. 2025, arXiv e-prints, arXiv:2509.00149. https://arxiv.org/abs/2509.00149

Allers, K. N., Vos, J. M., Biller, B. A., & Williams, P. K. G. 2020, Science, 368, 169, doi: 10.1126/science.aaz2856

Apai, D., Nardiello, D., & Bedin, L. R. 2021a, ApJ, 906, 64, doi: 10.3847/1538-4357/abcb97

—. 2021b, ApJ, 906, 64, doi: 10.3847/1538-4357/abcb97

Apai, D., Radigan, J., Buenzli, E., et al. 2013, ApJ, 768, 121, doi: 10.1088/0004-637X/768/2/121

Apai, D., Karalidi, T., Marley, M. S., et al. 2017, Science, 357, 683, doi: 10.1126/science.aam9848

Artigau, É., Bouchard, S., Doyon, R., & Lafrenière, D. 2009, ApJ, 701, 1534, doi: 10.1088/0004-637X/701/2/1534

Artigau, É., Doyon, R., Lafrenière, D., et al. 2006, ApJL, 651, L57, doi: 10.1086/509146

Astropy Collaboration, Robitaille, T. P., Tollerud, E. J., et al. 2013, A&A, 558, A33, doi: 10.1051/0004-6361/201322068

Astropy Collaboration, Price-Whelan, A. M., Sipőcz, B. M., et al. 2018, AJ, 156, 123, doi: 10.3847/1538-3881/aabc4f

Astropy Collaboration, Price-Whelan, A. M., Lim, P. L., et al. 2022, ApJ, 935, 167, doi: 10.3847/1538-4357/ac7c74

Barrow, C. H. 1960, Nature, 188, 924, doi: 10.1038/188924a0

Batalha, N. E., Marley, M. S., Lewis, N. K., & Fortney, J. J. 2019, ApJ, 878, 70, doi: 10.3847/1538-4357/ab1b51

Biller, B. A., Vos, J. M., Zhou, Y., et al. 2024, MNRAS, 532, 2207, doi: 10.1093/mnras/stae1602

Brown, Z. L., Medvedev, A. S., Starichenko, E. D., Koskinen, T. T., & Müller-Wodarg, I. C. F. 2022, Geophys. Res. Lett., 49, e97219, doi: 10.1029/2021GL097219

Burgasser, A. J., Liu, M. C., Ireland, M. J., Cruz, K. L., & Dupuy, T. J. 2008, ApJ, 681, 579, doi: 10.1086/588379

Burgasser, A. J., Marley, M. S., Ackerman, A. S., et al. 2002, ApJL, 571, L151, doi: 10.1086/341343

Burningham, B., Marley, M. S., Line, M. R., et al. 2017, MNRAS, 470, 1177, doi: 10.1093/mnras/stx1246

Burrows, A., Hubbard, W. B., Lunine, J. I., & Liebert, J. 2001, Reviews of Modern Physics, 73, 719, doi: 10.1103/RevModPhys.73.719

Chen, X., Biller, B. A., Tan, X., et al. 2025, MNRAS, 539, 3758, doi: 10.1093/mnras/staf737

Choi, D. S., Showman, A. P., Vasavada, A. R., & Simon-Miller, A. A. 2013, Icarus, 223, 832, doi: 10.1016/j.icarus.2013.02.001

Connerney, J. E. P., Kotsiaros, S., Oliversen, R. J., et al. 2018, Geophys. Res. Lett., 45, 2590, doi: 10.1002/2018GL077312

Connerney, J. E. P., Timmins, S., Joergensen, J. L., et al. 2022, in AGU Fall Meeting Abstracts, Vol. 2022, AGU Fall Meeting Abstracts, P32D–1857

Cowan, N. B., Fuentes, P. A., & Haggard, H. M. 2013, MNRAS, 434, 2465, doi: 10.1093/mnras/stt1191

Cowley, S. W. H., Bunce, E. J., & O'Rourke, J. M. 2004, Journal of Geophysical Research (Space Physics), 109, A05212, doi: 10.1029/2003JA010375

de Pater, I., Sault, R. J., Butler, B., DeBoer, D., & Wong, M. H. 2016, Science, 352, 1198, doi: 10.1126/science.aaf2210

Dobbs-Dixon, I., & Cowan, N. B. 2017, ApJL, 851, L26, doi: 10.3847/2041-8213/aa9bec

Doyon, R., Willott, C. J., Hutchings, J. B., et al. 2023, PASP, 135, 098001, doi: 10.1088/1538-3873/acd41b

Eriksson, S. C., Janson, M., & Calissendorff, P. 2019, A&A, 629, A145, doi: 10.1051/0004-6361/201935671

Faherty, J. K., Riedel, A. R., Cruz, K. L., et al. 2016, ApJS, 225, 10, doi: 10.3847/0067-0049/225/1/10

Faherty, J. K., Burningham, B., Gagné, J., et al. 2024, Nature, 628, 511, doi: 10.1038/s41586-024-07190-w

Filippazzo, J. C., Rice, E. L., Faherty, J., et al. 2015, ApJ, 810, 158, doi: 10.1088/0004-637X/810/2/158

Fletcher, L. N., Greathouse, T. K., Orton, G. S., et al. 2016, Icarus, 278, 128, doi: 10.1016/j.icarus.2016.06.008

Fletcher, L. N., Orton, G. S., Greathouse, T. K., et al. 2020, Journal of Geophysical Research (Planets), 125, e06399, doi: 10.1029/2020JE006399

Freytag, B., Allard, F., Ludwig, H. G., Homeier, D., & Steffen, M. 2010, A&A, 513, A19, doi: 10.1051/0004-6361/200913354

Fuda, N., Apai, D., Nardiello, D., et al. 2024, ApJ, 965, 182, doi: 10.3847/1538-4357/ad2c84

Gagné, J., Faherty, J. K., Burgasser, A. J., et al. 2017, ApJL, 841, L1, doi: 10.3847/2041-8213/aa70e2

Hallinan, G., Littlefair, S. P., Cotter, G., et al. 2015, Nature, 523, 568, doi: 10.1038/nature14619

Higson, E., Handley, W., Hobson, M., & Lasenby, A. 2019, Statistics and Computing, 29, 891, doi: 10.1007/s11222-018-9844-0

Hunter, J. D. 2007, Computing in Science & Engineering, 9, 90, doi: 10.1109/MCSE.2007.55

Ingersoll, A. P., Atreya, S., Bolton, S. J., et al. 2021, Geophys. Res. Lett., 48, e95756, doi: 10.1029/2021GL095756

Jakobsen, P., Ferruit, P., Alves de Oliveira, C., et al. 2022, A&A, 661, A80, doi: 10.1051/0004-6361/202142663

Kao, M. M., Hallinan, G., Pineda, J. S., et al. 2016, ApJ, 818, 24, doi: 10.3847/0004-637X/818/1/24

Kao, M. M., Hallinan, G., Pineda, J. S., Stevenson, D., & Burgasser, A. 2018, ApJS, 237, 25, doi: 10.3847/1538-4365/aac2d5

Kass, R. E., & Raftery, A. E. 1995, Journal of the American
Statistical Association, 90, 773,
doi: 10.1080/01621459.1995.10476572

Kim, S. J., Glenar, D. A., Joyce, R. R., & Kostiuk, T. 1993, Icarus,
102, 99, doi: 10.1006/icar.1993.1035

Lightkurve Collaboration, Cardoso, J. V. d. M., Hedges, C., et al.
2018, Lightkurve: Kepler and TESS time series analysis in
Python, Astrophysics Source Code Library.
http://ascl.net/1812.013

Lim, O., Benneke, B., Doyon, R., et al. 2023, ApJL, 955, L22,
doi: 10.3847/2041-8213/acf7c4

Liu, P., Biller, B. A., Vos, J. M., et al. 2024, MNRAS, 527, 6624,
doi: 10.1093/mnras/stad3502

Lothringer, J. D., Barman, T., & Koskinen, T. 2018, ApJ, 866, 27,
doi: 10.3847/1538-4357/aadd9e

Luger, R., Foreman-Mackey, D., Hedges, C., & Hogg, D. W. 2021,
AJ, 162, 123, doi: 10.3847/1538-3881/abfdb8

Marley, M. S., Saumon, D., Visscher, C., et al. 2021, ApJ, 920, 85,
doi: 10.3847/1538-4357/ac141d

McCarthy, A. M., Muirhead, P. S., Tamburo, P., et al. 2024, ApJ,
965, 83, doi: 10.3847/1538-4357/ad2c76

McCarthy, A. M., Vos, J. M., Muirhead, P. S., et al. 2025, ApJL,
981, L22, doi: 10.3847/2041-8213/ad9eaf

McKinney, W., et al. 2010, in Proceedings of the 9th Python in
Science Conference, Vol. 445, Austin, TX, 51–56

Melin, H., Stallard, T., Miller, S., et al. 2011, Geophys. Res. Lett.,
38, L15203, doi: 10.1029/2011GL048457

Mollière, P., Wardenier, J. P., van Boekel, R., et al. 2019, A&A, 627,
A67, doi: 10.1051/0004-6361/201935470

Morley, C. V., Marley, M. S., Fortney, J. J., et al. 2014, ApJ, 787, 78,
doi: 10.1088/0004-637X/787/1/78

Müller-Wodarg, I. C. F., Moore, L., Galand, M., Miller, S., &
Mendillo, M. 2012, Icarus, 221, 481,
doi: 10.1016/j.icarus.2012.08.034

Nasedkin, E., Mollière, P., & Blain, D. 2024, The Journal of Open
Source Software, 9, 5875, doi: 10.21105/joss.05875

Nasedkin, E., Schrader, M., Vos, J. M., et al. 2025, arXiv e-prints,
arXiv:2507.07772. https://arxiv.org/abs/2507.07772

Pineda, J. S., Hallinan, G., Desert, J.-M., & Harding, L. K. 2024,
ApJ, 966, 58, doi: 10.3847/1538-4357/ad2f9e

Plummer, M. 2024, Imber 3.0: Modeling Spectrophotometric
Variability of a Planetary-Mass Object, 3.0, Zenodo,
doi: 10.5281/zenodo.10729262

Plummer, M. K. 2023, Imber: Doppler imaging tool for modeling
stellar and substellar surfaces, Astrophysics Source Code Library,
record ascl:2307.033. http://ascl.net/2307.033

Plummer, M. K., & Wang, J. 2022, ApJ, 933, 163,
doi: 10.3847/1538-4357/ac75b9

—. 2023, ApJ, 951, 101, doi: 10.3847/1538-4357/accd5d

Plummer, M. K., Wang, J., Artigau, É., Doyon, R., & Suárez, G.
2024, ApJ, 970, 62, doi: 10.3847/1538-4357/ad4f89

Radigan, J. 2014, ApJ, 797, 120,
doi: 10.1088/0004-637X/797/2/120

Radigan, J., Lafrenière, D., Jayawardhana, R., & Artigau, E. 2014,
ApJ, 793, 75, doi: 10.1088/0004-637X/793/2/75

Reiners, A., & Basri, G. 2008, ApJ, 684, 1390, doi: 10.1086/590073

Robinson, T. D., & Marley, M. S. 2014, ApJ, 785, 158,
doi: 10.1088/0004-637X/785/2/158

Sandel, B. R., Shemansky, D. E., Broadfoot, A. L., et al. 1982,
Science, 215, 548, doi: 10.1126/science.215.4532.548

Sharan, S., Langlais, B., Amit, H., et al. 2022, Geophys. Res. Lett.,
49, e98839, doi: 10.1029/2022GL098839

Showman, A. P., & Kaspi, Y. 2013, ApJ, 776, 85,
doi: 10.1088/0004-637X/776/2/85

Showman, A. P., Tan, X., & Zhang, X. 2019, ApJ, 883, 4,
doi: 10.3847/1538-4357/ab384a

Skilling, J. 2004, in American Institute of Physics Conference
Series, Vol. 735, Bayesian Inference and Maximum Entropy
Methods in Science and Engineering: 24th International
Workshop on Bayesian Inference and Maximum Entropy
Methods in Science and Engineering, ed. R. Fischer, R. Preuss, &
U. V. Toussaint, 395–405, doi: 10.1063/1.1835238

Skilling, J. 2006, Bayesian Analysis, 1, 833, doi: 10.1214/06-BA127

Sorahana, S., Yamamura, I., & Murakami, H. 2013, ApJ, 767, 77,
doi: 10.1088/0004-637X/767/1/77

Speagle, J. S. 2020, MNRAS, 493, 3132,
doi: 10.1093/mnras/staa278

Suárez, G., & Metchev, S. 2022, MNRAS, 513, 5701,
doi: 10.1093/mnras/stac1205

Suárez, G., Vos, J. M., Metchev, S., Faherty, J. K., & Cruz, K. 2023,
ApJL, 954, L6, doi: 10.3847/2041-8213/acec4b

Suárez, G., Faherty, J. K., Burningham, B., et al. 2025, arXiv
e-prints, arXiv:2509.26505. https://arxiv.org/abs/2509.26505

Tan, X., & Showman, A. P. 2021a, MNRAS, 502, 678,
doi: 10.1093/mnras/stab060

—. 2021b, MNRAS, 502, 2198, doi: 10.1093/mnras/stab097

Tremblin, P., Amundsen, D. S., Chabrier, G., et al. 2016, ApJL, 817,
L19, doi: 10.3847/2041-8205/817/2/L19

Tremblin, P., Amundsen, D. S., Mourier, P., et al. 2015, ApJL, 804,
L17, doi: 10.1088/2041-8205/804/1/L17

Virtanen, P., Gommers, R., Oliphant, T. E., et al. 2020, Nature
Methods, 17, 261, doi: 10.1038/s41592-019-0686-2

Visscher, C., Lodders, K., & Fegley, Jr., B. 2010, ApJ, 716, 1060,
doi: 10.1088/0004-637X/716/2/1060

Visscher, C., & Moses, J. I. 2011, ApJ, 738, 72,
doi: 10.1088/0004-637X/738/1/72

Vos, J. M., Allers, K. N., & Biller, B. A. 2017, ApJ, 842, 78,
doi: 10.3847/1538-4357/aa73cf

Vos, J. M., Faherty, J. K., Gagné, J., et al. 2022, ApJ, 924, 68,
doi: 10.3847/1538-4357/ac4502

Vos, J. M., Burningham, B., Faherty, J. K., et al. 2023, ApJ, 944,
138, doi: 10.3847/1538-4357/acab58

Wright, G. S., Rieke, G. H., Glasse, A., et al. 2023, PASP, 135,
048003, doi: 10.1088/1538-3873/acbe66

Yang, H., Apai, D., Marley, M. S., et al. 2016, ApJ, 826, 8,
doi: 10.3847/0004-637X/826/1/8

Zhang, Z., Mollière, P., Fortney, J. J., & Marley, M. S. 2025, AJ,
170, 64, doi: 10.3847/1538-3881/addfcb

Zhou, Y., Bowler, B. P., Apai, D., et al. 2022, AJ, 164, 239,
doi: 10.3847/1538-3881/ac9905

Zhou, Y., Bowler, B. P., Morley, C. V., et al. 2020, AJ, 160, 77,
doi: 10.3847/1538-3881/ab9e04